Mapping total suspended matter from geostationary satellites: a feasibility study with SEVIRI in the Southern North Sea

Griet Neukermans[1,2,3,4,*], Kevin Ruddick[1], Emilien Bernard[5], Didier Ramon[5], Bouchra Nechad[1] and Pierre-Yves Deschamps[6]

[1]*Management Unit of the North Sea Mathematical Models (MUMM), Royal Belgian Institute for Natural Sciences (RBINS), Gulledelle 100, B-1200 Brussels, Belgium*
[2]*Université Lille Nord de France, F-59000 Lille, France*
[3]*ULCO, Laboratoire d'Océanologie et Géoscience (LOG), F-62930 Wimereux, France*
[4]*CNRS, UMR 8187, F-62930 Wimereux, France*
[5]*HYGEOS, Earth Observation, Avenue de Bretagne 165, 59000 Lille, France*
[6]*Laboratoire d'Optique Atmosphérique (LOA), Université de Lille 1, CNRS, F-59655 Villeneuve d'Ascq, France*
** g.neukermans@mumm.ac.be*

Abstract: Geostationary ocean colour sensors have not yet been launched into space, but are under consideration by a number of space agencies. This study provides a proof of concept for mapping of Total Suspended Matter (TSM) in turbid coastal waters from geostationary platforms with the existing SEVIRI (Spinning Enhanced Visible and InfraRed Imager) meteorological sensor on the METEOSAT Second Generation platform. Data are available in near real time every 15 minutes. SEVIRI lacks sufficient bands for chlorophyll remote sensing but its spectral resolution is sufficient for quantification of Total Suspended Matter (TSM) in turbid waters, using a single broad red band, combined with a suitable near infrared band. A test data set for mapping of TSM in the Southern North Sea was obtained covering 35 consecutive days from June 28 until July 31 2006. Atmospheric correction of SEVIRI images includes corrections for Rayleigh and aerosol scattering, absorption by atmospheric gases and atmospheric transmittances. The aerosol correction uses assumptions on the ratio of marine reflectances and aerosol reflectances in the red and near-infrared bands. A single band TSM retrieval algorithm, calibrated by non-linear regression of seaborne measurements of TSM and marine reflectance was applied. The effect of the above assumptions on the uncertainty of the marine reflectance and TSM products was analysed. Results show that (1) mapping of TSM in the Southern North Sea is feasible with SEVIRI for turbid waters, though with considerable uncertainties in clearer waters, (2) TSM maps are well correlated with TSM maps obtained from MODIS AQUA and (3) during cloud-free days, high frequency dynamics of TSM are detected.

OCIS codes: (280.0280) Remote Sensing and sensors; (010.0010) Atmospheric and oceanic optics; (010.1285) Atmospheric correction; (280. 4788) Optical sensing and sensors.

References and links

1. International Ocean Colour Coordinating Group (IOCCG), "Remote sensing of ocean colour in coastal, and other optically-complex waters," p. 140, IOCCG (2000).
2. R. P. Stumpf, "Applications of satellite ocean color sensors for monitoring and predicting harmful algal blooms," Human and Ecological Risk Assessment **7,** 1363-1368 (2001).
3. K. Ruddick, G. Lacroix, C. Lancelot, B. Nechad, Y. Park, S. Peters, B. Van Mol, "Optical remote sensing of the North Sea," in *Remote Sensing of the European Seas,* V. Barale and M. Gade [eds.], (Springer-Verlag, 2008) p 79-90.

#111963 - $15.00 USD Received 26 May 2009; revised 17 Jul 2009; accepted 17 Jul 2009; published 29 Jul 2009

4. I. S. Robinson, D. Antoine, M. Darecki, P. Gorringe, L. Pettersson, K. Ruddick, R. Santoleri, H. Siegel, P. Vincent, M. R. Wernand, G. Westbrook, and G. Zibordi, "Remote sensing of shelf sea ecosystems: state of the art and perspectives," European Science Foundation Marine Board p. 60, (2008).
5. G. Kang, S. Kang, S. Yong, J. Kim, Y. Chang, H. Youn, "Korea Geostationary Ocean Color Imager," IGARSS, IEEE (2004) p. 3261-3263.
6. National Research Council, *Earth Science andAapplications from Space: national imperatives for the next decade and beyond*, (Natl. Acad. Sci. 2007).
7. R. P. Stumpf and J. R. Pennock, "Calibration of a general optical equation for remote sensing of suspended sediments in a moderately turbid estuary," J. Geophysical Res. **94,** 14363-14371 (1989).
8. I. S. Robinson, *Satellite Oceanography* (Ellis Horwood Ltd., 1985).
9. E. Wolanski and S. Spagnol, "Dynamics of the turbidity maximum in King Sound, tropical Western Australia," Estuar Coast Mar Sci **56,** 877-890 (2003).
10. M. Fettweis, F. Francken, V. Pison, and D. Van Den Eynde, "Suspended particulate matter dynamics and aggregate sizes in a high turbidity area," Marine Geology **235,** 63-74 (2006).
11. W. Ebenhoeh, J. G. B. Bekker, and J. W. Baretta, "The primary production module in the marine ecosystem model ERSEM II, with emphasis on the light forcing," J. Sea Res. **38,** 173-193 (1997).
12. G. Lacroix, K. Ruddick, Y. Park, N. Gypens, and C. Lancelot, "Validation of the 3D biogeochemical model MIRO&CO with field nutrient and phytoplankton data and MERIS-derived surface chlorophyll *a* images," J. Mar. Syst. **64**(1-4), 66-88 (2007).
13. J. Muller, "MSG Level 1.5 Image Data Format Description. EUMETSAT technical document number EUM/MSG/ICD/105," (2007), http://www.eumetsat.int/Home/Main/Publications/Technical_and_Scientific_Documentation/Technical_Notes/SP_1124282611560 .
14. Y. Govaerts and M. Cleric, "MSG-1/SEVIRI Solar Channels Calibration Commissioning Activity Report. EUMETSAT document number EUM/MSG/TEN/04/0024," (2004).
15. D. Eisma, "The North Sea: an overview," Phil. Trans. R. Soc. Lond. B **316,** 461-485 (1987).
16. M. Fettweis, B. Nechad, et al, "An estimate of the suspended particulate matter (SPM) transport in the southern North Sea using SeaWiFS images, in situ measurements and numerical model results," Continental Shelf Research **27,** 1568-1583 (2007).
17. L. Otto, J. T. F. Zimmerman, et al., "Physical Oceanography of the North Sea," Netherlands J. Sea Res. **26,** 161-238 (1990).
18. M. Babin, D. Stramski, et al, "Variations in the light absorption coefficients of phytoplankton, nonalgal particles and dissolved organic matter in coastal waters around Europe," J. Geophys. Res. **108**(C7), 3211 (2003), doi:10.1029/2001JC000882.
19. W. Van Raaphorst, C. J. M. Philippart, et al, "Distribution of suspended particulate matter in the North Sea as inferred from NOAA/AVHRR reflectance images and in situ observations," J. Sea Res. **39,** 197-215 (1998).
20. R. Doerffer and J. Fischer, "Concentrations of chlorophyll, suspended matter, gelbstoff in case II waters derived from satellite coastal zone color scanner data with inverse modeling methods," J. Geophys. Res. **99**(C4), 7457-7466 (1994).
21. M. A. Eleveld, R. Pasterkamp, H. J. Van Der Woerd, "A survey of total suspended matter in the Southern North Sea based on 2001 SeaWiFS data," EARSeL eProceedings **3,** 166-178 (2004).
22. Y. Govaerts, S. Wagner, and M. Clerici, "SEVIRI native format pre-processing toolbox user's guide," issue: SPT version 2.2 Doc No: EUM/OPS-MSG/TEN/03/0011 (2005).
23. I. Reda and A. Andreas, "Solar position algorithm for solar radiation application," National Renewable Energy Laboratory (NREL), Technical report NREL/TP-560-34302 (2003).
24. J. M. Nicolas, P.-Y. Deschamps, O. Hagolle., "Radiometric calibration of the visible and near-infrared bands of SEVIRI using Rayleigh scattering and sun-glint over oceans," *Proceedings of the 3rd MSG RAO Workshop (ESA SP-619)*, 15 June 2006, Helsinki, Finland
25. M. Viollier, D. Tanré, and P.Y. Deschamps, "An algorithm for remote sensing of water color from space," Boundary Layer Meteorology **18,** 247-267 (1980).
26. H. R. Gordon and M. Wang, "Influence of oceanic whitecaps on atmospheric correction of ocean-color sensors," Appl. Opt. **33,** 7754-7763 (1994).
27. R. Frouin, M. Schwindling, and P. Y. Deschamps, "Spectral dependence of sea foam in the visible and near-infrared: In situ measurements and remote sensing implications," J. Geophys. Res. **101**(C6), 14361-14371 (1996).
28. E. F. Vermote, D. Tanre, J. L. Deuze, M. Herman, and J. J. Morcette, "Second Simulation of the Satellite Signal in the Solar Spectrum,6S: an overview," *IEEE Transaction on Geoscience and Remote Sensing,* Vol. **35**, Iss. 3, pp 675-686 (1997).
29. R. A. Mc Clatchey, R. W. Fenn, J. E. E. Selby, F. E. Volz, and J. S. Garing, "Optical properties of the Atmosphere," AFCRL-TR- 71-0279, Enviro. Research papers, No 354, L.G. HANCOM FIEL Bedford, Mass. U.S.A. (1971).
30. J. Lenoble, M. Herman, J. L. Deuzé, B. Lafrance, R. Santer, and D. Tanré, **"**A successive order of scattering code for solving the vector equation of transfer in the earths atmosphere with aerosols," J. Quant. Spectrosc. Radiat. Transfer **107,** 479-507 (2007).
31. E. P. Shettle and R. W. Fenn, "Models for the aerosols of the lower atmosphere and the effects of humidity variations on their optical properties," Air Force Geophysics Laboratory Environmental Research Papers No. 676, AFGL-TR-79-0214 (1979).

#111963 - $15.00 USD Received 26 May 2009; revised 17 Jul 2009; accepted 17 Jul 2009; published 29 Jul 2009

32. K. G. Ruddick, F. Ovidio, and M. Rijkeboer, "Atmospheric correction of SeaWiFS imagery for turbid coastal and inland waters," Appl. Opt. **39**(6), 897-912 (2000).
33. K. Ruddick, V. De Cauwer, Y. Park, and G. Moore, "Seaborne measurements of near infrared water-leaving reflectance: The similarity spectrum for turbid waters," Limnol. Oceanogr. **51**, 1167-1179, (2006).
34. B. Nechad, K. G. Ruddick, and Y. Park, "Calibration and validation of a generic multisensor algorithm for mapping of Total Suspended Matter in turbid waters," (subm. to Rem. Sens. Env.)
35. D. Eisma, "Supply and deposition of suspended matter in the North Sea," Spec. Publs int. Ass. Sediment **5,** 415-428 (1981).
36. P. M. Holligan, T. Aarup, and S. B. Groom, "The North Sea satellite colour atlas," Continental Shelf Research **9,** 665-765 (1989).
37. K. Ruddick, G. Lacroix, Y. Park, V. Rousseau, V. De Cauwer, and S. Sterckx, "Overview of Ocean Colour: theoretical background, sensors and applicability for the detection and monitoring of harmful algae blooms (capabilities and limitations)," p. 331-383. Real-time coastal observing systems for marine ecosystem dynamics and harmful algal blooms. Oceanographic Methodology Series. (UNESCO Publishing, 2008).
38. C. Mazeran and N. Meskini, "Mission Couleur de l'Océan Géostationaire: Charactérisation de la géométrie, gain en couverture, impact d'instabilites instrumentals," CNES-044-R650-RF-v1 ; 21 Octobre 2008 (2008).

1 Introduction

Since the launch of SeaWiFS in 1997 and MODIS-AQUA and ENVISAT-MERIS in 2002, ocean colour data from sensors on polar-orbiting platforms have become an established source of information for monitoring of chlorophyll *a* and total suspended matter (TSM) in coastal waters ([1-3]). These sensors provide data in mid-latitudes with typical space and time resolution of about 1km and 1 day in cloud-free periods. While these sensors give an enormous advantage in terms of spatial coverage when compared to *in situ* measurement techniques, cloudiness is a severe restriction in many regions. The daily revisit may also be a limitation in coastal waters with high frequency dynamics related to tide or wind-driven advection, resuspension or mixing/settling. For these two reasons the much higher temporal resolution that can be achieved from a geostationary platform is very attractive

The technology required for building geostationary platforms for optical sensors is well-established thanks to the METEOSAT and GOES (Geostationary Operational Environmental Satellite) series of meteorological sensors which have been operational since the 1970s. However, the higher orbit required for geostationary platforms increases greatly the cost as compared to polar-orbiting platforms and gives a reduction in spatial resolution for the same optical system. Notwithstanding the cost issue, and possible problems related to viewing geometry, the potential for geostationary ocean colour is theoretically very high ([4]) and plans for launching such sensors are at various stages of development within national and international space agencies ([5,6]). This study provides a proof of concept for TSM mapping from geostationary satellites in turbid coastal waters.

Although dedicated geostationary ocean colour sensors have not yet been launched into space, it is possible to test the application of TSM mapping in turbid waters with the existing SEVIRI sensor on the METEOSAT Second Generation platform (MSG). SEVIRI, with its few and broad spectral bands in the visible and near-infrared, is not capable of detecting chlorophyll. However, it has been established previously for the Advanced Very High Resolution Radiometer (AVHRR) sensor ([7]) that the use of a single broad red band, combined with a suitable near infrared band for aerosol correction, is sufficient for quantification of TSM in turbid waters. In fact, TSM concentration can be considered as quite an "easy" parameter to retrieve because of the strong signal: turbid regions can be identified from top of atmosphere radiance ([8]) or even in photographs taken from space ([9]). Mapping of TSM is of interest in many turbid regions because of its link with sediment transport problems (dredging, dumping, geomorphology) ([10]) and because of its impact on the availability of light for primary production ([11]). Remote sensing algorithms for TSM retrieval are now quite mature and satellite data is becoming more and more used in coastal monitoring and as support for modelling ([12]). TSM has therefore been adopted as the output parameter for this feasibility study.

The specific objectives of this study are to test the feasibility of mapping TSM in the Southern North Sea using the SEVIRI sensor and to determine whether high frequency

#111963 - $15.00 USD Received 26 May 2009; revised 17 Jul 2009; accepted 17 Jul 2009; published 29 Jul 2009

dynamics of TSM can be detected. The SEVIRI sensor, test data set and processing algorithms, including atmospheric correction and one-band TSM retrieval are briefly described. High frequency TSM dynamics are then presented for a cloud free day. Results show that (1) mapping of TSM in the Southern North Sea is feasible with SEVIRI in turbid waters, though with considerable uncertainties in clearer waters, (2) TSM maps are well correlated with TSM maps obtained from MODIS AQUA and (3) during cloud-free days, high frequency dynamics of TSM are detected. Finally, conclusions are drawn regarding the feasibility of geostationary sensors for mapping of TSM in coastal waters and recommendations are made for the design of future geostationary sensors for retrieval of both TSM and chlorophyll.

2 Materials and methods

2.1 SEVIRI instrument and test data set

The Spinning Enhanced Visible and InfraRed Imager (SEVIRI) radiometer ([13]) was primarily designed to support operational meteorology applications. It has 3 visible/near infrared and 8 thermal infrared channels with a spatial resolution at nadir of 3km and one visual broadband channel (HRV) where the spatial resolution at nadir is 1km. Spatial resolution in the VIS0.6 and VIS0.8 bands at 52°N is 4km (E-W direction) x 8km (N-S direction) ([13]). The nominal coverage is shown in Fig. 1. Data is available in near real time every 15 minutes and operationally processed to level 1.5 ([13]), *i.e.* corrected for radiometric and geometric non-linearity.

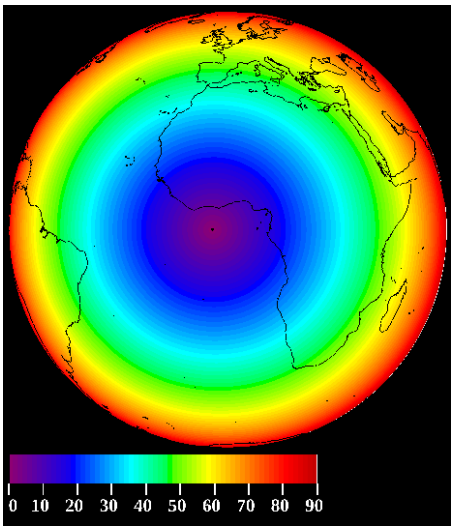

Fig. 1. Spatial extent of SEVIRI full disk imagery and viewing angle in degrees of SEVIRI on the MSG1-Meteosat8 platform located at 3.5°W.

The normalized spectral response function, ω(λ), for the 4 visible/near infrared bands of SEVIRI is shown in Fig. 2 ([14]). Two spectral band combinations were considered for mapping of suspended matter: the VIS0.6 (0.56-0.71μm, with central wavelength: $\lambda_0 = 0.635 \mu m$) and VIS0.8 (0.74-0.88μm, $\lambda_0 = 0.810 \mu m$) band pair and the VIS0.6 and NIR1.6 (1.50-1.78μm, $\lambda_0 = 1.640 \mu m$) band pair. An image test data set covering 35 consecutive days from June 28 until July 31 2006 was obtained.

#111963 - $15.00 USD Received 26 May 2009; revised 17 Jul 2009; accepted 17 Jul 2009; published 29 Jul 2009

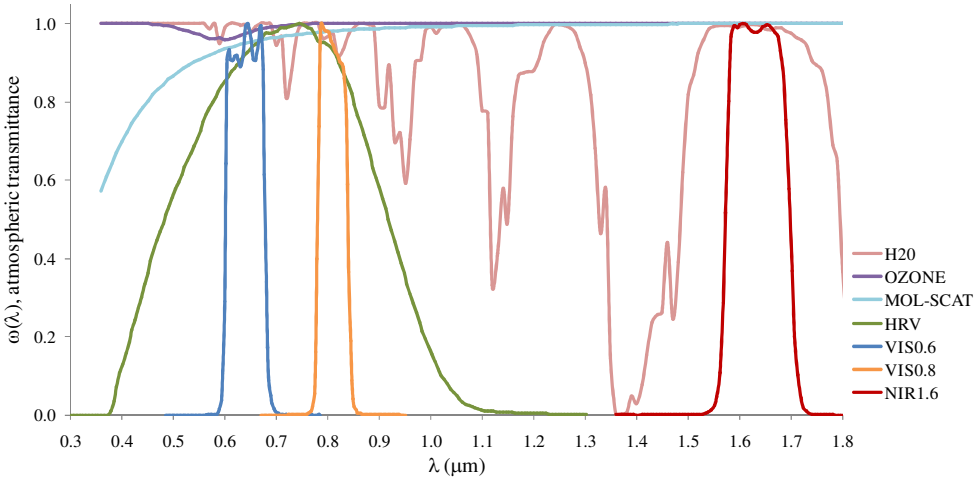

Fig. 2. Normalized spectral response, ω(λ), of the SEVIRI solar channels (source: [14]) and two-way atmospheric transmittances for water vapor, ozone and molecular scattering for a vertical atmospheric path and the US standard atmosphere model simulated with LOWTRAN.

2.2 Study area: SEVIRI subscene

The northern boundary of the study area corresponds to a maximum SEVIRI satellite viewing zenith angle of 64° and is shown in Fig. 3. For a location at the top of this subscene, total airmass (defined as $\cos(\theta_v)^{-1} + \cos(\theta_0)^{-1}$, where θ_v is the viewing zenith angle and θ_0 is the sun zenith angle) ranges between 3.4 and 5.4 over the timeframe 06:00-18:00UTC on June 30th 2006 (see Fig. 4). Rayleigh reflectances start to dominate the water-leaving signal for larger airmasses, rendering data unusable for ocean applications.

The area of the Southern North Sea and Western Channel chosen for this study is a relatively shallow sea region, with water depth mostly <50m, and is subject to strong semi-diurnal tidal currents e.g. with typical amplitude of 1 m/s. Suspended particulate matter originates from a variety of sources ([15]) including river discharges, inflow from the Atlantic Ocean ([16]), coastal and sea bottom erosion, atmospheric dust, primary production and dredging and mining operations. In the shallower near shore regions, tide and wind resuspension of bottom sediments is particularly important giving high TSM concentrations, even exceeding 100 mg/l, e.g. in some Belgian nearshore waters. The deeper offshore waters have generally much lower concentrations, down to 2 mg/l or less. Most of the region is vertically well-mixed except for some haline stratification along the Dutch coast and some thermal stratification in summer at the Northern limit of the domain ([17]). For most of this region TSM is not highly correlated with chlorophyll *a* – see Fig. 2(a) of ([18]). Optical remote sensing of TSM in this region has previously been achieved from a range of sensors including AVHRR ([19]), CZCS ([20]), SeaWiFS ([21]), MODIS and MERIS.

#111963 - $15.00 USD Received 26 May 2009; revised 17 Jul 2009; accepted 17 Jul 2009; published 29 Jul 2009

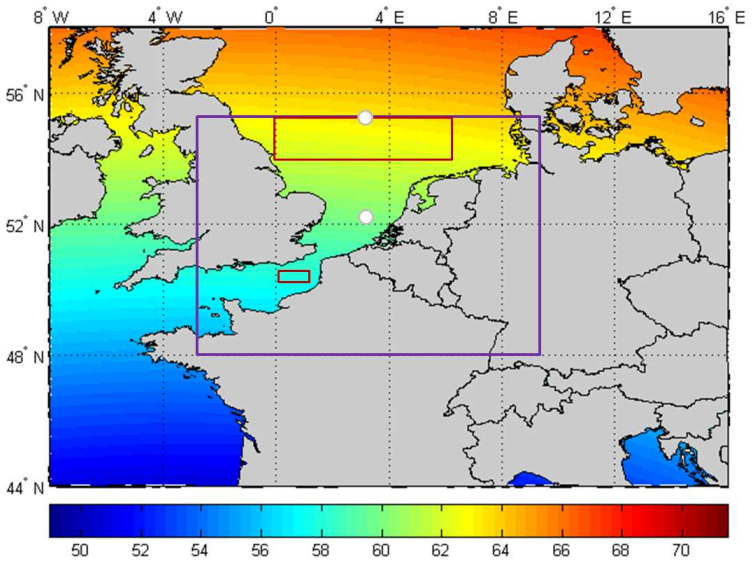

Fig. 3. Viewing angle of SEVIRI (on MSG1-Meteosat8 platform located at 3.5°W) over Western-Europe. The purple box delimits the study area, for which the northern limit corresponds to a 64° satellite viewing angle. The white dots are the locations for which daily variability of airmass and Rayleigh scattering are presented in Fig. 4. The red polygons bound the clear water pixels from which the ratio of aerosol reflectance $\varepsilon^{(6,8)}$ is obtained (see further in the text).

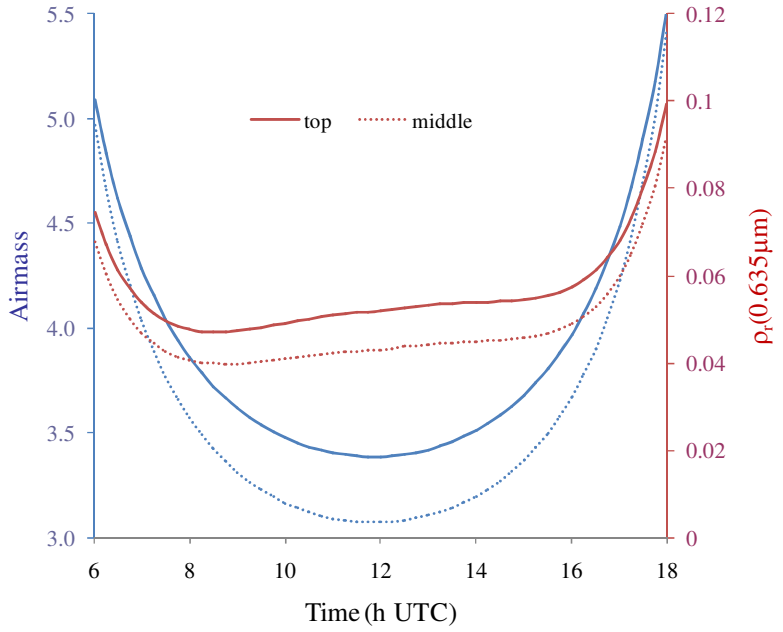

Fig. 4. Variability of Rayleigh reflectance for VIS0.6 (red lines) and total airmass (blue lines) on 29th June 2006 for two locations in the middle (dashed lines) and at the top (solid lines) of the SEVIRI subscene in Fig. 3.

#111963 - $15.00 USD Received 26 May 2009; revised 17 Jul 2009; accepted 17 Jul 2009; published 29 Jul 2009

2.3 Atmospheric correction of SEVIRI imagery

Solar radiation reflected by the ocean-atmosphere system to the SEVIRI sensor does not come uniquely from the sea. Depending on wavelength, geometry and water turbidity, between 35% and 95% of the measured light flux can have an atmospheric origin due to light scattering by air molecules and aerosols. These atmospheric influences need to be eliminated from the total signal at the top of the atmosphere (TOA) to obtain the marine reflectance (ρ_w), which is defined by multiplying the above water upwelling radiance L_w^{0+} by π and normalizing by the above-water downwelling irradiance E_d^{0+}, thus

$$\rho_w = \frac{\pi L_w^{0+}}{E_d^{0+}} \tag{1}$$

Total reflectance at TOA (ρ_{tot}^{TOA}) is obtained through calibration of SEVIRI level 1.5 data. Count data (K) are transformed into total radiance at TOA, L_{tot}^{TOA} [in $Wm^{-2}sr^{-1}\mu m^{-1}$] by applying the calibration coefficients (c_f) and offset values (r_0), provided with the SEVIRI level 1.5 native format file headers (see Table 1), as follows ([14]):

$$L_{tot}^{TOA} = \frac{10(c_f K + r_0)}{\lambda_0^2} \tag{2}$$

where λ_0 is the band central wavelength.

Total radiance at TOA, L_{tot}^{TOA} is then converted to total reflectance at TOA ([14]):

$$\rho_{tot}^{TOA} = \frac{\pi d^2 L_{tot}^{TOA}}{A_0 E_0 \cos\theta_0} \tag{3}$$

where d is the Sun-Earth distance in astronomical units (AU, [22]), θ_0 is the sun zenith angle calculated from position, date and time (MATLAB algorithm by [23]), E_0 is the extraterrestrial solar irradiance at TOA at 1AU (in $Wm^{-2}\mu m^{-1}$). Calibration correction factors for the SEVIRI solar channels, A_0, provided in [24], are applied to ρ_{tot}^{TOA} (see Table 1).

Table 1. Calibration parameters ([14]) and correction factors (A_0, [24]) for SEVIRI channels VIS0.6, VIS0.8 and NIR1.6

Channel	λ_0 (μm)	c_f ($mWm^{-2}sr^{-1}(cm^{-1})^{-1}$)	r_0 ($mWm^{-2}sr^{-1}(cm^{-1})^{-1}$)	E_0 ($Wm^{-2}\mu m^{-1}$)	A_0
VIS0.6	0.635	0.023128	-1.179533	1618.0	0.95
VIS0.8	0.810	0.029727	-1.516057	1113.0	0.95
NIR1.6	1.640	0.023622	-1.204717	231.9	1.09

The total reflectance at TOA, ρ_{tot}^{TOA} can be decomposed as follows ([25]):

$$\rho_{tot}^{TOA} = \rho_r^{TOA} + \rho_a^{TOA} + \rho_{wc}^{TOA} + \rho_g^{TOA} + T_0 T_v \rho_w \tag{4}$$

where ρ_r^{TOA} is the contribution to the reflectance from scattering by air molecules, ρ_a^{TOA} is the reflectance resulting from scattering by aerosols and from multiple scattering by aerosols and molecules. Both terms include photon interactions with the air-sea interface and are influenced by gaseous absorption. ρ_{wc}^{TOA} is the reflectance from foam and white caps and ρ_g^{TOA} is the contribution from sun glint for which the only scattering event is specular reflection of direct sunlight at the air-water interface. Sun glint reaches the sensor only for viewing zenith

#111963 - $15.00 USD Received 26 May 2009; revised 17 Jul 2009; accepted 17 Jul 2009; published 29 Jul 2009

angles (θ_v) close to the sun zenith (θ_0) and for relative azimuth angles between sun (φ_0) and sensor (ϕ_v) close to 180°. The SEVIRI relative azimuth angle ($|\varphi_0 - \varphi_v|$) varies between 2 and 75° and θ_v ranges between 55° and 64° over the entire study area and in the timeframe 08:00-16:00UTC. Measurements are clearly made outside the directions contaminated by sun glint and therefore ρ_g^{TOA} can be neglected. ρ_{wc}^{TOA} is small for wind speeds lower than 10 m/s and largely corrected for in the aerosol correction for maritime aerosols ([26]). The difference between the spectral variation of white caps ([27]) and aerosols gives an uncertainty on the marine reflectance of maximum 0.0009 for wind speeds of 10m/s. T_0 and T_v are the sun-sea and sea-sensor atmospheric transmittances, respectively. It is assumed that the effects of atmospheric gases (ozone, water vapour, methane, carbon dioxide), aerosols and air molecules, can be treated separately by decomposition of T_0 and T_v according to:

$$T_v = t_v^a t_v^r t_v^g \text{ and } T_0 = t_0^a t_0^r t_0^g$$

where t_0^a (t_v^a), t_0^r (t_v^r) are the sun-sea (sea-sensor) atmospheric transmittance factors for aerosol and Rayleigh effects and t_0^g (t_v^g) for absorption by atmospheric gases. Thus correcting Eq. (4) for the two-way gas transmittances and Rayleigh transmittances (assuming that marine aerosols are generally low in the atmosphere) gives:

$$\rho_{tot}^{\prime TOA} = \rho_r^{\prime TOA} + \rho_a^{\prime TOA} + t_{0,v}^a \rho_w \tag{5}$$

where $t_{0,v}^a = t_0^a t_v^a$ and $\rho' = \frac{\rho}{t_0^g t_v^g t_0^r t_v^r}$. For notational simplicity, the prime symbols and TOA notation are dropped hereafter. The gaseous absorption correction is performed using the Msixs software package, based on 6S code by [28]. This allows the computation of the transmittances of ozone, and water vapour in the VIS0.6 and VIS0.8 bands and for CO_2 and CH_4 in the NIR1.6 band.

The correction for absorption by water vapour, which is strong in the VIS0.8 band (see Fig. 2), is done using the precipitable water content (PWC) obtained from the National Weather Service's National Centers for Environmental Prediction (NCEP) meteorological data. PWC can be quite variable during the day, therefore, PWC data is obtained at four times during the day at 0:00, 6:00, 12:00 and 18:00 UTC and linearly interpolated in between. Ozone column content is obtained from AIRS (1.0° x 1.0° daily Level-3 product) through NASA's Giovanni application, and daily averaged over the study area. CO_2 and CH_4 concentrations are obtained from climatological values for these gas vertical profiles (Mid latitude summer atmospheric model, [29]). Then, the 6S software is used to simulate the transmittances of these two gases for different airmasses. Finally a second order polynomial interpolation of the transmittances as a function of airmass is applied to derive the CO_2 and CH_4 transmittances within the field of view of SEVIRI.

The Rayleigh scattering component, ρ_r, and two-way Rayleigh transmittances, $t_0^r t_v^r$ are calculated from geometry (sun and sensor zenith and azimuth angles), atmospheric pressure and wind speed using lookup tables constructed from the Successive Order of Scattering code ([30]). Atmospheric pressure and wind speed are spatially averaged over the study area from 6-hourly NCEP atmospheric pressure data. A daily mean pressure is computed, while a temporal nearest neighbour is taken for wind speeds. The Rayleigh corrected reflectance is defined as:

$$\rho_c = \rho_{tot} - \rho_r = \rho_a + t_{0,v}^a \rho_w \tag{6}$$

#111963 - $15.00 USD Received 26 May 2009; revised 17 Jul 2009; accepted 17 Jul 2009; published 29 Jul 2009

To obtain ρ_w, the aerosol reflectance ρ_a and the two-way aerosol transmittances, $t_{0,v}^a$, remain to be computed. ρ_a can be computed wherever the water reflectance is negligible, *i.e.* typically in the clearest case 1 waters. However, for other waters further knowledge or assumptions are required regarding the spectral behaviour of ρ_a, which varies with aerosol size and refractive index. To obtain ρ_w in the VIS0.6 band, $\rho_w^{(0.6)}$, two approaches are considered using either the VIS0.8 or NIR1.6 band to correct for aerosol scattering. This is discussed in Appendix A and shows that the (VIS0.6, VIS0.8) band pair minimizes the uncertainty on the desired $\rho_w^{(0.6)}$. This band pair is therefore selected for the processing described hereafter.

The relations and unknown quantities are, after Eq. (6):

$$\rho_c^{(0.6)} = \rho_a^{(0.6)} + t_{0,v}^{a(0.6)} \rho_w^{(0.6)} \tag{7}$$

$$\rho_c^{(0.8)} = \rho_a^{(0.8)} + t_{0,v}^{a(0.8)} \rho_w^{(0.8)} \tag{8}$$

where $\rho_c^{(0.6)}$ and $\rho_c^{(0.8)}$ are given for each image pixel and the other six parameters ($\rho_a^{(0.6)}, \rho_a^{(0.8)}, \rho_w^{(0.6)}, \rho_w^{(0.8)}, t_{0,v}^{a(0.6)}$ and $t_{0,v}^{a(0.8)}$) are unknown. For each aerosol model ([31]), the following quantities are obtained from look-up tables (LUT):

1. LUT_{ra}: aerosol reflectance as a function of viewing and illumination geometry, wavelength and aerosol optical thickness,
2. LUT_{ta}: aerosol transmittances as a function of zenith angle, wavelength and aerosol optical thickness.

The two-way aerosol transmittances $t_{0,v}^{a(0.6)}$ and $t_{0,v}^{a(0.8)}$ can thus be obtained from viewing and illumination geometries and aerosol optical thickness via LUT_{ta}, where the aerosol optical thickness in turn can be obtained from the aerosol reflectance look-up table (LUT_{ra}) "inversion" as follows:

1. compute aerosol reflectance corresponding to aerosol optical thicknesses of 0.05 and 0.5 from LUT_{ra},
2. linearly interpolate the observed aerosol reflectance over the aerosol reflectance range obtained from 1 to obtain the corresponding aerosol optical thickness. Values outside this range are considered clouds and masked.

The system now has 4 equations (Eq. (7), Eq. (8), $t_{0,v}^{a(0.6)} = LUT_{ta} \circ LUT_{ra}^{-1}(\rho_a^{(0.6)})$ and $t_{0,v}^{a(0.8)} = LUT_{ta} \circ LUT_{ra}^{-1}(\rho_a^{(0.8)}))$ with 6 unknowns. To close the system, further assumptions regarding the spectral shape of aerosol and marine reflectances are needed. In this study the following assumptions are made:

1. The ratio of marine reflectances in bands VIS0.6 and VIS0.8 is assumed to be a constant value in space and time:

$$\sigma = \frac{\rho_w^{(0.6)}}{\rho_w^{(0.8)}} \tag{9}$$

A similar assumption was made previously for the SeaWiFS 765nm and 865nm bands ([32]). For the SEVIRI bands this assumption is less valid for very turbid waters. The consequences for the TSM products are discussed later.

2. The ratio of aerosol reflectance in bands VIS0.6 and VIS0.8 is assumed to be spatially homogeneous over the subscene of interest:

$$\varepsilon^{(6,8)} = \frac{\rho_a^{(0.6)}}{\rho_a^{(0.8)}} \tag{10}$$

#111963 - $15.00 USD Received 26 May 2009; revised 17 Jul 2009; accepted 17 Jul 2009; published 29 Jul 2009

The marine reflectance ratio (σ) is calibrated from an extensive archive of *in situ* above-water marine reflectance measurements collected between 2001 and 2006 with a set of TriOS Ramses radiometers. From a total of 440 reflectance measurements, 46 measurements were selected with clear skies, low wind speeds and small deviation from the time-averaged mean reflectance at 780nm to calibrate σ (for details see [33]).

The SEVIRI band reflectances were then obtained as follows:

$$\rho_w^{(0.6)} = \pi \frac{\int_{\lambda \in VIS\,0.6} L_w^{0+}(\lambda)\omega(\lambda)d\lambda}{\int_{\lambda \in VIS\,0.6} E_d^{0+}(\lambda)\omega(\lambda)d\lambda} \quad (11)$$

These remaining 46 ($\rho_w^{(0.8)}, \rho_w^{(0.6)}$) reflectance measurements are shown in Fig. 5. The relationship between $\rho_w^{(0.8)}$ and $\rho_w^{(0.6)}$ becomes non-linear for higher reflectances. The parameter σ is calibrated through linear regression of 33 reflectance measurements for which $\rho_w^{(0.8)}$ <0.011. For our dataset, this limitation of the model does not pose great problems, since $\rho_w^{(0.8)}$ only rarely exceeds 0.011. Moreover, the very turbid water points represented by the triangles in Fig. 5 generally correspond to near-shore waters (less than 3 km from the Belgian coast), which are not mapped due to the coarse spatial resolution of SEVIRI. Refinement of this algorithm would be needed for application to higher TSM concentration waters.

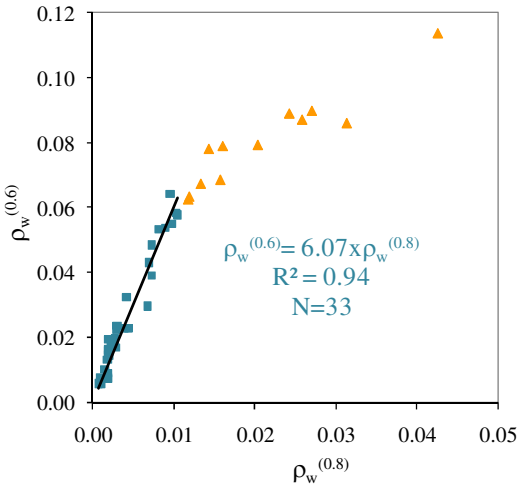

Fig. 5. Marine reflectances in the VIS0.6 and VIS0.8 bands obtained from optimal *in situ* above-water marine reflectance measurements collected between 2001 and 2006 in Southern North Sea waters. The parameter σ is calibrated through linear regression (black line) of 33 reflectance measurements for which $\rho_w^{(0.8)}$ <0.011.

The ratio of aerosol reflectance $\varepsilon^{(6,8)}$ is obtained on an image-by-image basis from the ratio of Rayleigh and gas corrected reflectances for SEVIRI bands VIS0.6 and VIS0.8 over clear waters pixels (shown in the red polygons in Fig. 3). The distribution of these reflectance ratios is approximately normal (see example in Fig. 6). For every SEVIRI scene, $\varepsilon^{(6,8)}$ is estimated automatically from the mean and the uncertainty on $\varepsilon^{(6,8)}$ is quantified from two times the standard deviation (see Appendix A). Fig. **6** shows some discretisation effects coming from digitisation of the top of atmosphere signal which is of the order 0.0013 for the VIS0.6 channel and 0.0015 for the VIS0.8 channel. For every SEVIRI scene, the aerosol

#111963 - $15.00 USD Received 26 May 2009; revised 17 Jul 2009; accepted 17 Jul 2009; published 29 Jul 2009

Angström coefficient (related to aerosol type and size distribution) is obtained from $\varepsilon^{(6,8)}$ as follows:

$$\alpha = \frac{-\ln(\varepsilon^{(6,8)})}{\ln\left(\frac{0.635}{0.810}\right)} \tag{12}$$

Based on α, a nearest neighbour approach is then used to select the most appropriate aerosol model from the model set ([31]).

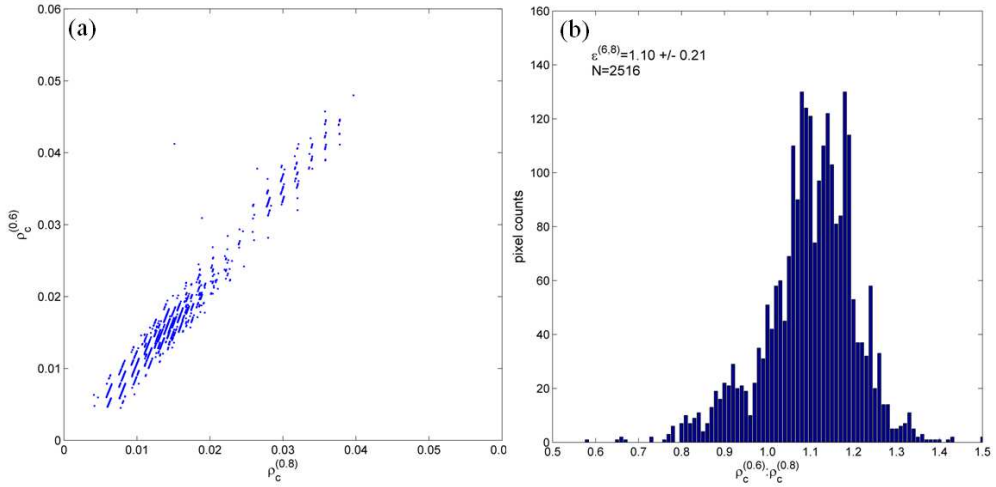

Fig. 6. Estimation of VIS0.6:VIS0.8 ratio of aerosol reflectances. (a) Rayleigh corrected reflectances for a set of clear water pixels in VIS0.6 and VIS0.8 bands on June 29th 2006 at 11:30UTC. (b) The corresponding histogram of the VIS0.6:VIS0.8 Rayleigh corrected reflectance ratios (N is the number of pixels).

Using Eq. (9):

$$t_{0,v}^{a(0.6)}\rho_w^{(0.6)} = \frac{t_{0,v}^{a(0.6)}}{t_{0,v}^{a(0.8)}} t_{0,v}^{a(0.8)}\sigma\rho_w^{(0.8)} = \gamma\sigma t_{0,v}^{a(0.8)}\rho_w^{(0.8)} \tag{13}$$

where the VIS0.6:VIS0.8 ratio of two-way aerosol transmittances (γ).is given by:

$$\gamma = \frac{t_{0,v}^{a(0.6)}}{t_{0,v}^{a(0.8)}} \tag{14}$$

Using Eq. (13) and Eq. (10), the system (Eq. (7)-(8)) can now be rewritten:

$$\varepsilon^{(6,8)}\rho_a^{(0.8)} + \gamma\sigma t_{0,v}^{a(0.8)}\rho_w^{(0.8)} = \rho_c^{(0.6)} \tag{15}$$

$$\rho_a^{(0.8)} + t_{0,v}^{a(0.8)}\rho_w^{(0.8)} = \rho_c^{(0.8)} \tag{16}$$

which can be solved by substitution to give:

$$\rho_a^{(0.8)} = \frac{\gamma\sigma\rho_c^{(0.8)} - \rho_c^{(0.6)}}{\gamma\sigma - \varepsilon^{(6,8)}} \tag{17}$$

#111963 - $15.00 USD Received 26 May 2009; revised 17 Jul 2009; accepted 17 Jul 2009; published 29 Jul 2009

$$\rho_w^{(0.8)} = \frac{\rho_c^{(0.6)} - \varepsilon^{(6,8)}\rho_c^{(0.8)}}{t_{0,v}^{a(0.8)}(\gamma\sigma - \varepsilon^{(6,8)})} \tag{18}$$

$$\rho_a^{(0.6)} = \varepsilon^{(6,8)}\frac{\gamma\sigma\rho_c^{(0.8)} - \rho_c^{(0.6)}}{\gamma\sigma - \varepsilon^{(6,8)}} \tag{19}$$

$$\rho_w^{(0.6)} = \sigma\frac{\rho_c^{(0.6)} - \varepsilon^{(6,8)}\rho_c^{(0.8)}}{t_{0,v}^{a(0.8)}(\gamma\sigma - \varepsilon^{(6,8)})} \tag{20}$$

γ remains unknown, until after computation of the aerosol reflectances (from Eq. (17) and Eq. (19)). Therefore, a two-pass algorithm was used: first setting $\gamma = 1$ and solving Eq. (17) and Eq. (19), yielding a second approximation of γ, which is then used to solve Eq. (17) and Eq. (19) and give a second, final estimate of $\rho_a^{(0.6)}$ and $\rho_a^{(0.8)}$.

2.4 Single band TSM algorithm.

The single band TSM retrieval algorithm of ([34]) is of the following form:

$$TSM = \frac{A\rho_w^{(0.6)}}{C - \rho_w^{(0.6)}} + B \tag{21}$$

and has been recalibrated here for the VIS0.6 band from an archive of 63 seaborne reflectance and TSM measurements, giving the coefficients *A*=38.02, *B*=2.32 mg/l and *C*=0.162 ([34]). Uncertainties on the calibrations of the *A* and *B* coefficients, obtained from their 95% confidence intervals are 5.28 and 2.65, respectively.

The semi-empirically derived algorithm is shown in Fig. 7. Radiative transfer simulation with Hydrolight 4.2 gives a reflectance at 0.635µm of 0.00028 for pure sea water with no suspended particles, implying a theoretical offset of *B*=-0.07 mg/l. The non-zero offset found above is specific to the *in situ* measurements used for calibration. Since any offset for the SEVIRI instrument and processing is likely to be very different from the *in situ* measurement bias, the algorithm is applied here without the offset *B*.

For some pixels in clear waters, $\rho_w^{(0.6)}$ was found to be negative (up to -0.01). This is thought to be typical of the uncertainty of the method, including all aspects of atmospheric correction and sensor calibration. For these pixels, TSM concentration was set to 0 mg/l.

#111963 - $15.00 USD Received 26 May 2009; revised 17 Jul 2009; accepted 17 Jul 2009; published 29 Jul 2009

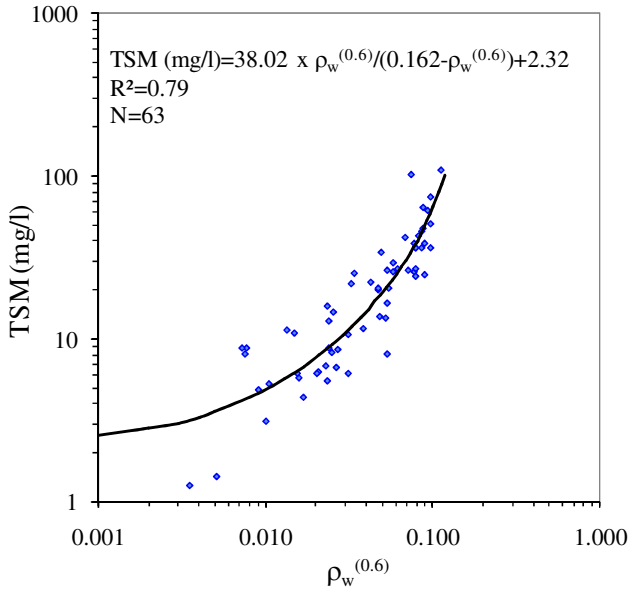

Fig. 7. Regression between 63 *in situ* reflectance measurements of $\rho_w^{(0.6)}$ and TSM concentration obtained from ship borne measurements in the Southern North Sea between 2001 and 2006.

2.5 Estimation of uncertainties on the derived products

As derived in Appendix A, the uncertainty on the marine reflectance in the VIS0.6 band associated with the uncertainties on the key assumptions of spatial homogeneity of VIS0.6:VIS0.8 band ratios of aerosol and marine reflectance (Eq. (9) and Eq. (10)) is given by Eq. (A4):

$$\Delta\rho_w^{(0.6)} = \frac{1}{t_{0,v}^{a(0.8)}}\left[\left(\frac{\rho_a^{(0.8)}\sigma}{(\gamma\sigma-\varepsilon^{(6,8)})}\Delta\varepsilon^{(6,8)}\right)^2+\left(\frac{\rho_w^{(0.8)}\varepsilon^{(6,8)}t_{0,v}^{a(0.8)}}{\gamma\sigma-\varepsilon^{(6,8)}}\Delta\sigma\right)^2\right]^{1/2} \quad (22)$$

The important contributions to this uncertainty can be seen more clearly by simplifying with $t_{0,v}^{a,r(0.8)}=1$ and $\gamma=1$, to give:

$$\Delta\rho_w^{(0.6)} \approx \left[\left(\rho_a^{(0.8)}\frac{\sigma}{\sigma-\varepsilon^{(6,8)}}\Delta\varepsilon^{(6,8)}\right)^2+\left(\rho_w^{(0.8)}\frac{\varepsilon^{(6,8)}\Delta\sigma}{\sigma-\varepsilon^{(6,8)}}\right)^2\right]^{1/2} \quad (23)$$

For typical values of the North sea, $\varepsilon^{(6,8)}=1.1\pm0.3$ and $\sigma=6.1\pm0.3$, the first component equals $0.37\,\rho_a^{(0.8)}$, while the second component equals $0.07\ \rho_w^{(0.8)}$ and represents the uncertainty caused by Eq. (10) and Eq. (9), respectively.

The uncertainty on TSM, due to uncertainties in the aerosol correction, as derived in Appendix A (Eq. (A11)) is given by:

$$\Delta TSM = \left|\frac{AC\Delta\rho_w^{(0.6)}}{(C-\rho_w^{(0.6)})^2}\right| \quad (24)$$

2.6 Processing steps: from SEVIRI Level 1.5 data to TSM concentration

The atmospheric correction is schematically depicted in Fig. 8 and can be summarized as follows:

#111963 - $15.00 USD Received 26 May 2009; revised 17 Jul 2009; accepted 17 Jul 2009; published 29 Jul 2009

1. Calibrate SEVIRI level 1.5 data to obtain ρ_{tot}^{TOA} in VIS0.6 and VIS0.8 SEVIRI channels from Eq. (2) and Eq. (3)
2. Correct for gaseous absorption, Rayleigh transmittance (Eq. (5)) and Rayleigh scattering (Eq. (6))
3. Compute the calibration parameter $\varepsilon^{(6,8)}$ from the ratio of Rayleigh and gas corrected reflectances for SEVIRI bands VIS0.6 and VIS0.8 over clear waters pixels in every scene (Eq. (10)), estimate $\Delta\varepsilon^{(6,8)}$ from Eq. (A2)
4. Compute α from Eq.(12) and determine the aerosol model ([31])
5. Compute $\rho_a^{(0.8)}$ and $\rho_a^{(0.6)}$ from Eq. (17) and Eq. (19), first setting $\gamma = 1$
6. Get $\tau_a^{(0.8)}$ and $\tau_a^{(0.6)}$ from $\rho_a^{(0.6)}$ and $\rho_a^{(0.8)}$, respectively through linear interpolation of ρ_a over the interval [0.05 0.5] as described in the text between (Eq. (8) and Eq. (9))
7. Get $t_{0,v}^{a(0.8)}$ and $t_{0,v}^{a(0.6)}$ from the t^a-LUT
8. Repeat steps (5)-(7) with $\gamma = \dfrac{t_{0,v}^{a(0.6)}}{t_{0,v}^{a(0.8)}}$
9. Compute $\rho_w^{(0.8)}$ and $\rho_w^{(0.6)}$ from Eq. (18) and Eq. (20)
10. Apply the single band TSM algorithm to $\rho_w^{(0.6)}$ using Eq. (21), set TSM=0 for $\rho_w^{(0.6)}$ <0
11. Compute $\Delta\rho_w^{(0.6)}$ from Eq. (22) and ΔTSM from Eq. (24)

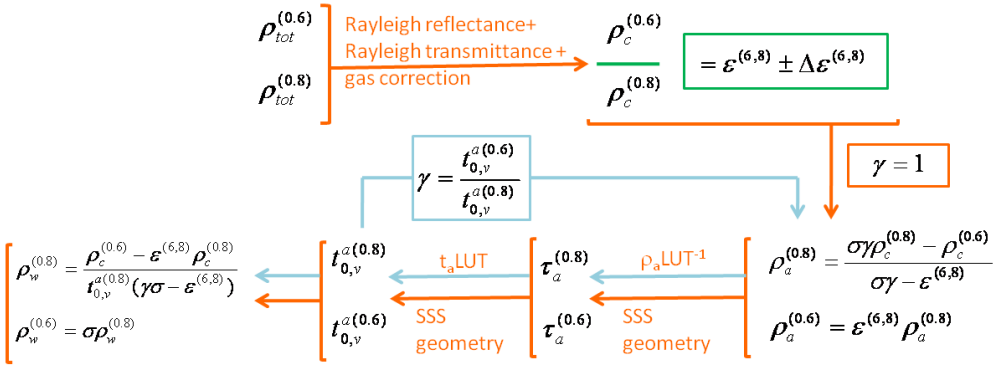

Fig. 8. Schematical depiction of the processing steps in the atmospheric correction of the SEVIRI VIS0.6 and VIS0.8 channels (SSS= sun-sea-satellite). The second pass in the two-pass algorithm is represented by the blue lines (in the first pass, shown by the orange lines, $\gamma = 1$).

2.7 Cross-validation

SEVIRI TSM products were cross-validated with cloud free MODIS AQUA TSM products on 4 days: June 29th 2006 at 12:45 UTC, July 15th at 12:45 UTC, July 17th at 12:35 UTC and July 18th at 13:15 UTC.

TSM maps from MODIS were obtained by application of the TSM retrieval algorithm of [34] in Eq. (21) (where *A*=62.86 , *C*=0.1736 and *B*=0) to the MODIS 667nm band. MODIS TSM images were resampled to the larger SEVIRI grid where the spatial average and standard deviation of TSM values were computed in a 3x3 pixel box surrounding the MODIS pixel with coordinates corresponding to the SEVIRI pixel centre coordinates. A linear regression analysis of MODIS TSM values against SEVIRI TSM values was made. Points with zero

#111963 - $15.00 USD Received 26 May 2009; revised 17 Jul 2009; accepted 17 Jul 2009; published 29 Jul 2009

TSM values for either sensor (from negative marine reflectances) where omitted in the regression analysis.

3 Results and discussion

3.1 TSM concentration mapping

Fig. **9** (top panel) shows TSM concentrations in the Southern North Sea obtained from SEVIRI on June 29th at 13:00 UTC. These distributions are similar to those found in many previous studies based on *in situ* measurements, e.g. [34], or satellite measurements from CZCS ([36]), AVHRR ([19]), SeaWiFS ([21]), MODIS or MERIS ([37]). Moderate and high TSM concentration (>10mg/l) are found in some areas close to the continental coast of Europe and near river estuaries and especially East of the Thames Estuary, e.g. (51.5°N, 1.5°E). TSM concentrations are lower (<10mg/l) offshore in the Central North Sea and the English Channel. The bottom panel in Fig. 9 shows the uncertainty on the derived TSM concentration associated with uncertainties in the atmospheric correction (obtained from Eq. (24)). TSM concentration ranges between 0 and 34mg/l, with 14 out of 8704 pixels exceeding concentrations of 23mg/l. For these pixels the assumption on the ratio of marine reflectances in bands VIS0.6 and VIS0.8 is less valid (see Eq. (9) and Fig. 5). Absolute uncertainties in TSM concentration (see bottom panel in Fig. 9) range between 0.03 and 9.6mg/l. Uncertainties are highest near clouds and near the coast, due to strong atmospheric turbidity (high aerosol scattering). For turbid waters with TSM concentrations above 10mg/l, relative uncertainties range between 4 and 51% (108 pixels, 2 outliers removed, with a mean uncertainty of 20±10%). Moderately turbid waters, with TSM concentrations between 5 and 10mg/l (167 pixels, 2 outliers removed), are mapped with an average accuracy of 32±18%, ranging between 2 and 86%. Zero TSM concentrations were found for 3274 pixels, with absolute uncertainties between 0.4 and 5.2mg/l. For the clearer waters, with TSM concentrations between 0 and 1mg/l (3705 pixels), relative uncertainties generally exceed 100% and such concentrations must be considered as below the detection limit of this method.

#111963 - $15.00 USD Received 26 May 2009; revised 17 Jul 2009; accepted 17 Jul 2009; published 29 Jul 2009

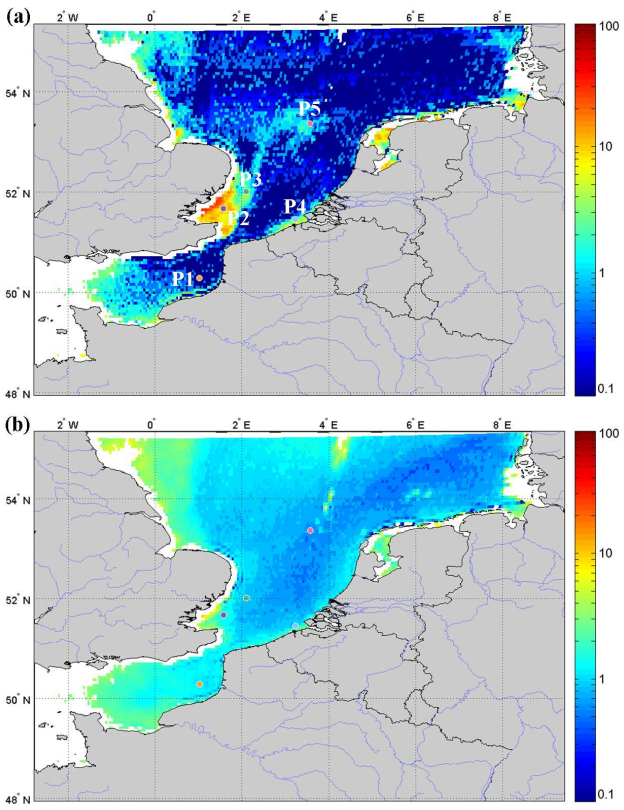

Fig. 9. (a) (Media 1) TSM (mg/l) concentration in the Southern North Sea from SEVIRI on June 29th 2006 at 13:00 UTC. Five pixels P1-P5 were selected in clear and turbid waters for which high frequency TSM dynamics are presented in Fig. 12). (b) Estimated aerosol correction uncertainty on TSM concentration (from Eq. (24)). White areas are clouds or have aerosol optical thicknesses higher than 0.5. Grey areas are land.

The TSM map given in Fig. 9 shows considerable spatial noise in the low concentration regions. This was traced to corresponding digitisation noise in the top of atmosphere reflectance data, which was of the order of 0.0013 for the VIS0.6 channel. This can be translated approximately to noise in the TSM map by multiplying by the factor A/C, giving 0.305mg/l.

3.2 Cross-validation of TSM maps

Fig. **10** shows a spatial comparison between SEVIRI TSM and MODIS TSM maps, acquired simultaneously on July 18th 2006. These products show comparable spatial patterns and comparable TSM concentration ranges but the SEVIRI image is clearly affected by spatial noise and lacks the spatial resolution necessary to pick up the finer spatial structures seen in the MODIS image. A cross-validation analysis was performed between corresponding TSM products and the resulting regression is shown in Fig. 11. The error bars for MODIS TSM show the standard deviation from the spatial mean obtained from downsampling the MODIS pixels to the SEVIRI grid. The error bars for SEVIRI TSM show the estimated uncertainty on the TSM value as obtained from Eq. (24). A good correlation was found with a correlation coefficient of 0.91 and a coefficient of determination, R^2, of 0.83. Similar correlation coefficients were found for the other 3 match-ups on June 29th at 12:45 UTC, July 15th at 12:45 UTC and July 17th at 12:35 UTC (see Table 2). It is noted that the slope of the regression line is close to one and that the offsets are close to zero. Discrepancies between the two datasets could be caused by differences in atmospheric correction, differences between

#111963 - $15.00 USD Received 26 May 2009; revised 17 Jul 2009; accepted 17 Jul 2009; published 29 Jul 2009

SEVIRI and MODIS AQUA bandwidth and central wavelengths and differences in spatial resolution.

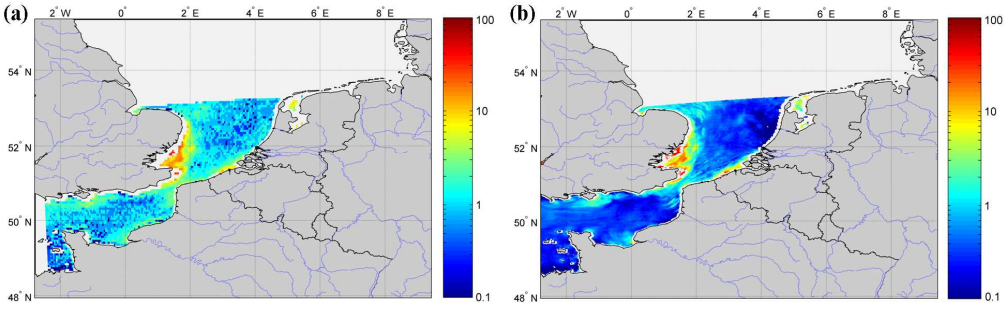

Fig. 10. TSM (mg/l) maps obtained from SEVIRI (a) and MODIS (b) on July 18th 2006 at 13:15 UTC.

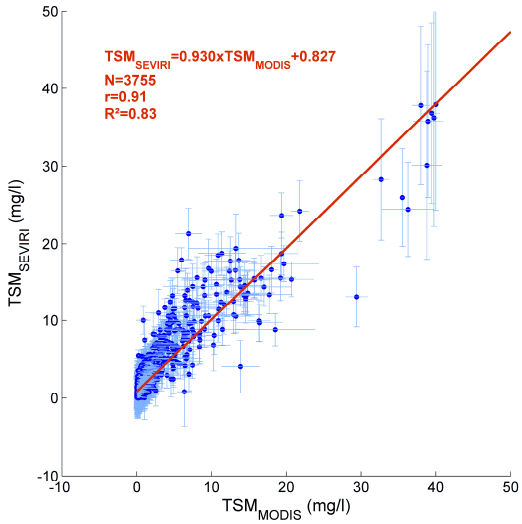

Fig. 11. Regression of TSM (mg/l) obtained from MODIS and from SEVIRI on July 18th 2006 at 13:15 UTC. The error bars for MODIS TSM show the standard deviation from the spatial mean obtained from downsampling the MODIS pixels to the SEVIRI grid. The error bars for SEVIRI TSM show the estimated uncertainty on the TSM value assicated with the aerosol correction and computed from Eq. (24). Zero TSM values were omitted.

Table 2. Statistics of the regression analysis between TSM (mg/l) obtained from MODIS and from SEVIRI.

Date	Regression equation	N	r	R^2
29/06/2006, 12:45UTC	TSM_{SEVIRI}=0.851 TSM_{MODIS}-0.423	5321	0.881	0.776
15/07/2006, 12:45UTC	TSM_{SEVIRI}=0.876 TSM_{MODIS} +0.299	6675	0.850	0.722
17/07/2006, 12:35UTC for MODIS, 12:30UTC for SEVIRI	TSM_{SEVIRI}=0.841 TSM_{MODIS} -0.352	5358	0.826	0.681
18/07/2006, 13:15UTC	TSM_{SEVIRI}=0.930 TSM_{MODIS} +0.827	3755	0.910	0.827

3.3 High frequency TSM dynamics

The high frequency variability of TSM concentration is studied on a cloudfree day on June 29th 2006 at five different pixels/stations (shown in the top panel of Fig. 9) in clear, moderately turbid and turbid waters of the Southern North Sea: P1 (50.28°N, 1.03°E) offshore of Boulogne and P5 (53.37°N, 3.58°E) in the Middle of the North Sea, P3 (52.01°N, 2.10°E)

#111963 - $15.00 USD Received 26 May 2009; revised 17 Jul 2009; accepted 17 Jul 2009; published 29 Jul 2009

offshore of Lowestoft, P4 (51.45°N, 3.23°E) close to the mouth of the river Scheldt (moderately turbid water), and P2 (51.67°N, 1.57°E) in turbid water. Time series of TSM concentration and their uncertainties were extracted at these five pixels between 8:00 and 16:00 UTC and are shown in Fig. 12.

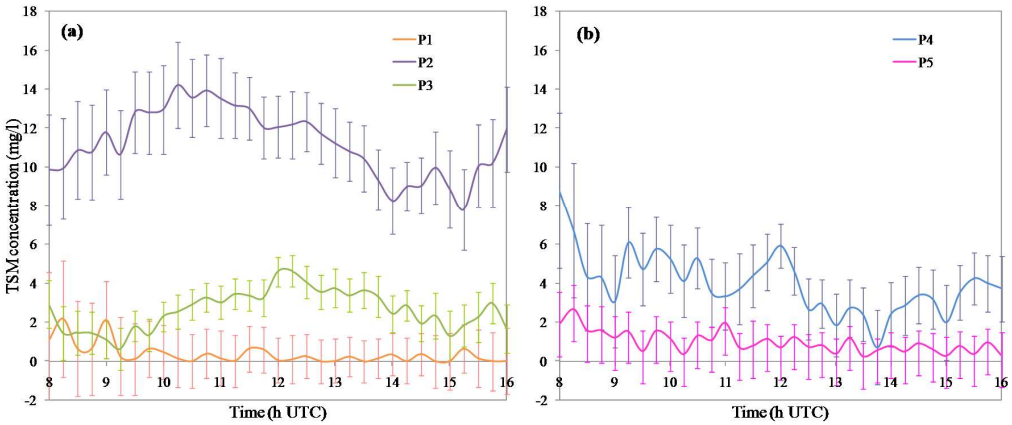

Fig. 12. High frequency variability of TSM concentration at P1-P3 (a) and P4-P5 (b) on a cloudfree day (June 29th 2006). The error bars denote the estimated uncertainty on the TSM concentration arising from the aerosol correction and as expressed by Eq. (24).

For P1, TSM concentrations are close to zero. The absolute uncertainty on these low concentrations ranged between 1.0 and 3.5 mg/l, with a mean of 1.5±0.6mg/l. Uncertainties on TSM concentrations for P2 ranged between 12 and 29%, while TSM concentration varies by a factor 2 over an 8h period. Between 10:00 and 14:15 UTC, relative uncertainties for P3 ranged between 16 and 34%, but increased above 45% outside that timeframe due to atmospheric turbidity. For P4, relative uncertainties of 19 to 96% were found. Relative uncertainties ranged between 39 and over 100% at P5. The variability of TSM concentration in the coastal pixels P2 and P3 suggests a periodicity related to the tidal cycle, such as could be expected from resuspension/settling and/or advection. At the other stations, possible diurnal variability cannot be discerned due to the high noise level. The period and the spatial variability of the amplitude and phase of this high frequency variability in turbid waters will be analysed with a more complete dataset and in conjunction with hydrodynamical model results in a future study.

4 Conclusion and future prospects

Though the geostationary meteorological SEVIRI radiometer, with its few and broad spectral bands, high radiometric noise level and medium ground resolution, is not designed for ocean colour remote sensing, this study demonstrates the feasibility of this sensor for TSM concentration mapping in the Southern North Sea. It is shown that TSM products from SEVIRI are highly correlated with similar data from MODIS. Also, SEVIRI TSM uncertainties in turbid waters are comparable to MODIS TSM uncertainties, though, in clear waters SEVIRI TSM uncertainties are very high due to radiometric noise and/or digitization effects.

The striking advantage of SEVIRI is the superior temporal resolution: every 15 minutes compared to once per day for MODIS. This study provides the basis for future mapping of TSM from geostationary sensors at very high temporal resolution. Important applications of the availability of very high temporal resolution TSM maps include:

1. Mitigating the problems of cloudiness encountered with the current generation of polar-orbiters (MODIS, MERIS, SeaWiFS), through daily averaging of the SEVIRI images in areas of low TSM variability.

#111963 - $15.00 USD Received 26 May 2009; revised 17 Jul 2009; accepted 17 Jul 2009; published 29 Jul 2009

2. Studying high frequency dynamics of the coastal ecosystem: resuspension of bottom sediments, horizontal tidal advection, possible diurnal biological processes (migration etc.)
3. Identifying areas of high frequency variability of TSM, indicating where the SeaWiFS /MODIS/ MERIS daily products are less reliable and providing a daily average TSM and standard deviation.

The atmospheric correction procedure developed in this study can easily be expanded to almost the entire SEVIRI disk (shown in Fig. 1) during the whole year. Some considerations:

1. Total air mass should not exceed 4-5, therefore, TSM mapping in e.g. the Southern North Sea will become more problematic in winter with low sun angles and TSM mapping will possibly be limited to 10:00 – 14:00 UTC
2. Spatial resolution in areas closer to the SEVIRI nadir point will be finer than the North Sea area (4km x 8km) and can be up to 3km at Nadir
3. Digitization and/or radiometric noise from the sensor is clearly a problem, particularly for low concentration TSM regions and for low sun angles.
4. The TSM algorithm presented in this study is calibrated for North Sea waters and its applicability to other waters remains to be investigated. A TSM retrieval algorithm applied to the SEVIRI full disk imagery could allow detecting high frequency TSM dynamics in some of the world's major estuaries, like the Amazon and the Congo River deltas.
5. The geostationary geometry limits sunglint problems to equatorial areas (generally between 10°S and 10°N) where the sunglint spot moves from East to West along with the sun's position ([38]).

The SEVIRI processing could be extended to a higher spatial resolution by use of the panchromatic visual band (1kmx1km at nadir). This would require further refinement of both the atmospheric correction and the TSM retrieval algorithms.

If temporal variability is highly correlated in space it is a very attractive prospect to combine synergistically the high temporal frequency offered by SEVIRI with the higher spatial resolution offered by sensors such as MODIS-250m, MERIS-300m, SPOT, etc.

The potential of SEVIRI to observe high frequency dynamics of TSM is shown. Future geostationary satellite sensors with ocean color capability, like GOCI and GEO-CAPE, will offer the opportunity to study short-scale temporal variability of other marine parameters, such as chlorophyll. High airmass may be more problematic for blue/green bands than for the SEVIRI VIS0.6 and VIS0.8 bands. However, there should be no significant algorithmic difficulties since the methodology for polar-orbiting sensors is easily transported to geostationary sensors – the stable geostationary viewing geometry even simplifies some aspects of atmospheric correction. The potential for geostationary ocean colour is both enormous ([4]) and is now clearly feasible.

Appendix A

An estimate of the uncertainties associated with the assumptions on the ratios of waterleaving reflectances and aerosol reflectances in the red and near-infrared bands (Eq. (9) and Eq. (10) in the main text) on the desired $\rho_w^{(0.6)}$ is made in this Appendix. Other possible sources of uncertainties, such as sensor calibration, whitecap correction, aerosol model, radiometric noise, Rayleigh correction, etc. are not considered because the objective here is to isolate the errors associated with the key assumptions in Eq. (9) and Eq. (10) in the main text. Two band combinations are considered for atmospheric correction: (VIS0.6, VIS0.8) or (VIS0.6, NIR1.6).

1 Estimation of uncertainty on $\rho_w^{(0.6)}$ using band combination (VIS0.6, VIS0.8)

In the first case where the VIS0.8 band is used as correction band (and where $\rho_w^{(0.8)} > 0$ for turbid waters), we adopt the atmospheric correction procedure of SeaWiFS imagery for turbid

#111963 - $15.00 USD Received 26 May 2009; revised 17 Jul 2009; accepted 17 Jul 2009; published 29 Jul 2009

waters by Ruddick *et al.* (2000). This approach is based on two assumptions: Eq. (9) and Eq. (10) in the main text.

First, we estimate the uncertainty on the ratio of marine reflectances in bands VIS0.6 and VIS0.8. The least squares estimator of the slope of a line of the form y=ax through a cloud of points (xi,yi) is:

$$\hat{a} = \frac{\sum x_i y_i}{\sum x_i^2}$$

with variance:

$$S_a^2 = \frac{1}{(n-1)\sum x_i^2}\left(\sum y_i^2 - \frac{\left(\sum x_i y_i\right)^2}{\sum x_i^2}\right)$$

and thus, the uncertainty on the slope is $\Delta a = 2\sqrt{S_a^2}$.

Applying the above formulae to the $\left(\rho_w^{(0.8)}, \rho_w^{(0.6)}\right)$ dataset of in-situ reflectances gives:

$$\sigma = 6.1 \pm 0.3 \tag{A1}$$

Now, we estimate the uncertainty associated with the second assumption: the ratio of aerosol scattering in bands VIS0.6 and VIS0.8. The aerosol reflectance ratio $\varepsilon^{(6,8)}$ for SEVIRI bands VIS0.6 and VIS0.8 can be derived from the ratio of Rayleigh and gas corrected reflectances in the VIS0.6 and VIS0.8 bands, when only clear water pixels are considered (2350 pixels). The reflectance ratio histogram approaches a normal distribution and $\varepsilon^{(6,8)}$ is then estimated as the mean, with an estimated uncertainty of 2 standard deviations:

$$\varepsilon^{(6,8)} = \hat{\varepsilon}^{(6,8)} \pm 2\sqrt{S^2_{\varepsilon^{(6,8)}}} \tag{A2}$$

The uncertainties on the key assumptions of spatial homogeneity of VIS0.6:VIS0.8 band ratios of aerosol and marine reflectance (Eq. (9) and Eq. (10) in the main text) have an effect on the accuracy of the derived marine reflectance in the VIS0.6 band. Other sources of error, like sensor calibration, whitecap correction, aerosol-Rayleigh interactions, aerosol model, etc. are not considered here, because the aim is to isolate the effect of the key assumptions on the derived products. So, the uncertainties on the calibration factors (σ and $\varepsilon^{(6,8)}$) introduce an uncertainty in the marine reflectance $\rho_w^{(0.6)}$. When $\Delta\sigma$ and $\Delta\varepsilon^{(6,8)}$ are the uncertainties in the estimation of the calibration parameters σ and $\varepsilon^{(6,8)}$ respectively, then the consequent uncertainty in marine reflectance in band VIS0.6 is:

$$\Delta\rho_w^{(0.6)} = \left[\left(\frac{\partial\rho_w^{(0.6)}}{\partial\sigma}\Delta\sigma\right)^2 + \left(\frac{\partial\rho_w^{(0.6)}}{\partial\varepsilon^{(6,8)}}\Delta\varepsilon^{(6,8)}\right)^2\right]^{1/2} \tag{A3}$$

Using $\rho_w^{(0.6)}$ from Eq. (20) , $\rho_a^{(0.8)}$ from Eq. (17) and $\rho_w^{(0.8)}$ from Eq. (18), gives:

$$\Delta\rho_w^{(0.6)} = \frac{1}{t_{0,v}^{a(0.8)}}\left[\left(\frac{\rho_a^{(0.8)}\sigma}{(\gamma\sigma - \varepsilon^{(6,8)})}\Delta\varepsilon^{(6,8)}\right)^2 + \left(\frac{\rho_w^{(0.8)}\varepsilon^{(6,8)}t_{0,v}^{a(0.8)}}{\gamma\sigma - \varepsilon^{(6,8)}}\Delta\sigma\right)^2\right]^{1/2} \tag{A4}$$

#111963 - $15.00 USD Received 26 May 2009; revised 17 Jul 2009; accepted 17 Jul 2009; published 29 Jul 2009

2 Estimation of uncertainty on $\rho_w^{(0.6)}$ using band combination (VIS0.6, NIR1.6)

In the second case where the NIR1.6 band is used as correction band we assume zero marine reflectance in NIR1.6 and spatial homogeneity of aerosol scattering:

$$\rho_a^{(1.6)} = \rho_c^{(1.6)} \tag{A5}$$

$$\varepsilon^{(6,16)} = \frac{\rho_a^{(0.6)}}{\rho_a^{(1.6)}} \tag{A6}$$

In analogy with the derivation of $\Delta\rho_w^{(0.6)}$ using the (VIS0.6, VIS0.8) band pair, we estimate the uncertainty on the marine reflectance $\rho_w^{(0.6)}$, resulting from an uncertainty on the estimation of the calibration parameter $\varepsilon^{(6,16)}$:

$$\Delta\rho_w^{(0.6)} = \left|\frac{\partial\rho_w^{(0.6)}}{\partial\varepsilon^{(6,16)}}\Delta\varepsilon^{(6,16)}\right| = \frac{1}{t_{0,v}^{a(0.6)}}\left|\frac{\partial\rho_a^{(0.6)}}{\partial\varepsilon^{(6,16)}}\Delta\varepsilon^{(6,16)}\right| = \frac{\rho_a^{(1.6)}}{t_{0,v}^{a(0.6)}}\Delta\varepsilon^{(6,16)} \tag{A7}$$

The ratio of aerosol reflectance $\varepsilon^{(6,16)}$ is obtained on an image-by-image basis from the ratio of Rayleigh and gas corrected reflectances for SEVIRI bands VIS0.6 and NIR1.6 over clear waters pixels (same pixels as for the VIS0.6, VIS0.8 band pair). The distribution of these reflectance ratios is approximately normal (see example in Fig. 13). $\varepsilon^{(6,16)}$ is estimated from the mean and the uncertainty on $\varepsilon^{(6,16)}$ is quantified from two times the standard deviation (Eq. (A2)). Fig. 13 shows some discretisation effects coming from digitisation of the top of atmosphere signal and is of the order 0.0013 for the VIS0.6 channel and 0.0014 for the NIR1.6 channel. Typical values for $\varepsilon^{(6,16)}$ are 3.4±2.4.

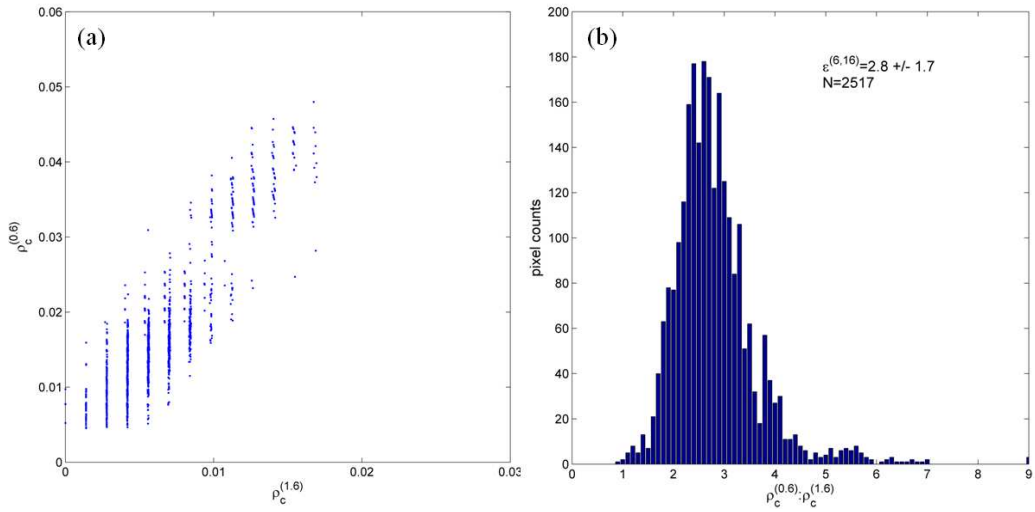

Fig. 13. Estimation of VIS0.6:NIR1.6 ratio of aerosol reflectances. (a) Rayleigh corrected reflectances for a set of clear water pixels in VIS0.6 and NIR1.6 bands on June 29th 2006 at 11:30UTC. (b) The corresponding histogram of the VIS0.6:NIR1.6 Rayleigh corrected reflectance ratios (N is the number of pixels).

#111963 - $15.00 USD Received 26 May 2009; revised 17 Jul 2009; accepted 17 Jul 2009; published 29 Jul 2009

3 Band pair selection based on minimizing $\Delta\rho_w^{(0.6)}$

The purpose is to find the band pair that minimizes $\Delta\rho_w^{(0.6)}$, obtained from Eq. (A4) and Eq. (A7) for the (VIS0.6,VIS0.8) and (VIS0.6, NIR1.6) band pairs respectively.

We evaluate $\Delta\rho_w^{(0.6)}$ in Table 1 using values typical of the Southern North Sea: $t_{0,v}^{a,r,(0.6)}=1$, $\varepsilon^{(6,8)}=1.1\pm0.3$, $\varepsilon^{(6,16)}=3.1\pm2.1$, $\sigma=6.1\pm0.3$, with an aerosol optical thickness $\tau_a^{(0.8)}$ between 0.05 (clear atmosphere) and 0.50 (turbid atmosphere) and $\rho_w^{(0.8)}$ varying from 0.001 (clear water) to 0.010 (turbid water). The $\rho_a^{(0.8)}$ values corresponding to different values of $\tau_a^{(0.8)}$ are obtained from the T90-aerosol look-up table for sun-sea-satellite geometry values typical for SEVIRI: $\theta_v=60°, \varphi=60°$ and the sun at zenith. $\rho_a^{(1.6)}$ is then obtained from:

$$\rho_a^{(1.6)}=\rho_a^{(0.8)}\frac{\rho_a^{(0.6)}}{\rho_a^{(0.8)}}\frac{\rho_a^{(1.6)}}{\rho_a^{(0.6)}}=\rho_a^{(0.8)}\frac{\varepsilon^{(6,8)}}{\varepsilon^{(6,16)}} \tag{A8}$$

Table 3. Estimation of uncertainties on $\rho_w^{(0.6)}$ associated with assumptions (Eq. (9) and Eq. (10) in the main text) for the (VIS0.6,VIS0.8) band pair and assumption (Eq. (A5) and Eq. (A6)) for the (VIS0.6,NIR1.6) band pair, obtained from Eq. (A4) and Eq. (A7) respectively. Values typical of the Southern North Sea were used: $\varepsilon^{(6,8)}=1.1\pm0.3$, $\varepsilon^{(6,16)}=3.1\pm2.1$, $\sigma=6.1\pm0.3$, $\tau_a^{(0.8)}$ between 0.05 and 0.5 and $\rho_w^{(0.8)}$ between 0.001 and 0.010. Some simplifications: $t_{0,v}^{a,r,(0.6)}=1$, $\gamma=1$. Estimated uncertainties on TSM concentration obtained from Eq. (A11) are also shown.

			$\rho_w^{(0.8)}$	$\rho_w^{(0.6)}$	TSM (mg/l)
	Water	clear	0.001	0.006	1.488
		mod. turbid	0.005	0.031	8.818
		turbid	0.010	0.061	22.963
			$\tau_a^{(0.8)}$	$\rho_a^{(0.8)}$	$\rho_a^{(1.6)}$
	Atmosphere	very clear	0.05	0.004	0.002
		clear	0.10	0.008	0.003
		turbid	0.20	0.017	0.006
		very turbid	0.50	0.047	0.017
			Water		
			clear	mod. turbid	turbid
$\Delta\rho_w^{(0.6)}$ **(VIS0.6,VIS0.8)**	Atmosphere	very clear	0.0015	0.0015	0.0016
		clear	0.0031	0.0031	0.0031
		turbid	0.0063	0.0063	0.0063
		very turbid	0.0171	0.0171	0.0171
ΔTSM **(VIS0.6,VIS0.8)**	Atmosphere	very clear	0.3826	0.5499	0.9941
		clear	0.7784	1.1000	1.8964
		turbid	1.6003	1.2522	3.8334
		very turbid	4.3369	6.0968	10.3408
			All water types		
$\Delta\rho_w^{(0.6)}$ **(VIS0.6,NIR1.6)**	Atmosphere	very clear	0.0031		
		clear	0.0063		
		turbid	0.0129		
		very turbid	0.0348		

Table 1 shows that the estimated uncertainties on $\rho_w^{(0.6)}$ when derived from the (VIS0.6, NIR1.6) band pair are in all cases of atmosphere and water turbidities approximately a factor

#111963 - $15.00 USD Received 26 May 2009; revised 17 Jul 2009; accepted 17 Jul 2009; published 29 Jul 2009

2 larger than the uncertainties on $\rho_w^{(0.6)}$ when derived from the (VIS0.6, VIS0.8) band pair. We note that, for the (VIS0.6, NIR1.6) band pair, the estimated uncertainty on $\rho_w^{(0.6)}$ is independent of water turbidity. Clearly, the (VIS0.6, VIS0.8) band pair is the preferred band combination, resulting in much smaller uncertainties on the derived $\rho_w^{(0.6)}$.

4 Uncertainty on TSM

The uncertainty on TSM, resulting from uncertainties on $\rho_w^{(0.6)}$ (Eq. (A4)) from the atmospheric correction and the parameter *A* will then be:

$$\Delta TSM = \frac{1}{C - \rho_w^{(0.6)}} \left[\left(\rho_w^{(0.6)} \Delta A \right)^2 + \left(\frac{AC\Delta\rho_w^{(0.6)}}{C - \rho_w^{(0.6)}} \right)^2 \right]^{1/2} \quad \text{(A9)}$$

With relative uncertainty

$$\frac{\Delta TSM}{TSM} = \left[\left(\frac{C\Delta\rho_w^{(0.6)}}{C - \rho_w^{(0.6)}} \right)^2 + \left(\frac{\Delta A}{A} \right)^2 \right]^{1/2} \quad \text{(A10)}$$

where $\frac{\Delta A}{A} = 0.14$.

The two components in the expression for the relative uncertainty on TSM (Eq. (A10)) have a very different nature. The second component is the uncertainty arising from the TSM algorithm calibration (Eq. (21) in the main text) and is equal to 14% everywhere in the scene. Uncertainties in the TSM algorithm calibration are caused by various factors such as *in situ* measurement uncertainties for reflectances and TSM concentrations and uncertainties in the reflectance-TSM model including natural variability of the particulate backscatter/TSM ratio. For a more extensive discussion on the TSM algorithm and uncertainties in calibration, see Nechad et al. (2009). The first component is the atmospheric correction uncertainty arising from uncertainties on the assumptions on the ratios of waterleaving reflectances and aerosol reflectances in the red and near-infrared bands (Eq. (9) and Eq. (10) in the main text), and is roughly proportional to the aerosol reflectance. The part of Eq. (A9) due to atmospheric correction is:

$$\Delta TSM = \left| \frac{AC\Delta\rho_w^{(0.6)}}{(C - \rho_w^{(0.6)})^2} \right| \quad \text{(A11)}$$

ΔTSM (from Eq. (A11)) is evaluated in the lower half of Table 1. For turbid waters, uncertainties between 4% and 45% are expected, while for clear waters, uncertainties can exceed 200% in the case of very turbid atmospheres.

Acknowledgements

This research was supported by the BELCOLOUR-2 project, funded by the STEREO programme of the Belgian Science Policy Office under contract SR/00/104. The NASA Ocean Color Product Distribution at GSFC is acknowledged for providing and distributing MODIS products. MUMM's Chemistry Laboratory is acknowledged for the analysis of TSM data. The crew of the Belgica research vessel is thanked for their kind help during sea campaigns. Thanks to Nicholas Clerbeaux for providing SEVIRI data and kind help. Emannuel Boss and researchers from the Laboratoire d'Océanographie de Villefranche are thanked for their useful comments on this paper. The first author is involved in a MUMM-ULCO collaborative PhD

research project. Her promoter, Hubert Loisel, is thanked for his support. Two anonymous reviewers are thanked for their helpful comments on the manuscript.

#111963 - $15.00 USD Received 26 May 2009; revised 17 Jul 2009; accepted 17 Jul 2009; published 29 Jul 2009